Copyright © 2014 by American Scientific Publishers
All rights reserved.
Printed in the United States of America

AMERICAN SCIENTIFIC PUBLISHERS

Science of Advanced Materials
Vol. 6, pp. 1160–1169, 2014
(www.aspbs.com/sam)

One-Step Synthesis, Structural and Optical Characterization of Self-Assembled ZnO Nanoparticle Clusters with Quench-Induced Defects

Bharati Debnath[†], **Ganga Halder**[†], **and Sayan Bhattacharyya**[*]

Department of Chemical Sciences, Indian Institute of Science Education and Research,
Kolkata, Mohanpur 741252, Nadia, W.B., India

ABSTRACT

The applications of zinc oxide (ZnO) nanostructures require tuning of the defect levels which govern their optical properties. Self-assembled 8–10 nm ZnO nanoparticle clusters with different defect concentration were prepared by thermal decomposition of zinc acetate dihydrate at 900 °C and subsequent quenching in air, ice and liquid nitrogen. The cell volume and quench-induced structural disorder proportionately increased with larger temperature difference between 900 °C and the quenching media. Multi-peak fitting of the photoluminescence (PL) spectra showed that only zinc interstitials and zinc vacancies were present without any oxygen vacancy. Multiple violet emissions were attributed to the energy levels associated with interface trap in the grain boundaries and dislocations. The three quenched samples showed higher intensity of the defect bands as compared to pristine ZnO. Electron transfer to carbon nanowhiskers was facilitated by the defect bands at the lowest energy levels associated with the grain boundaries, dislocations and surface traps.

Delivered by Publishing Technology to: Sayan Bhattacharyya
IP: 14.139.220.33 On: Wed, 08 Oct 2014 09:24:41
Copyright: American Scientific Publishers

KEYWORDS: Zinc Oxide, Nanoparticle, Quenching, Rietveld Analysis, Photoluminescence.

1. INTRODUCTION

Defect states in semiconductor nanostructures play a pivotal role in guiding the charge carriers and their optoelectronic properties.[1] One of the elite and widely studied semiconductors is ZnO with potential technological applications in lasers,[2] sensors,[3] solar cells,[4] field-emission devices,[5,6] spintronics,[7,8] photocatalysis,[9] ceramics,[10] and as UV protector.[11] It has the more stable hexagonal wurtzite structure with space group $P6_3mc$, and less stable cubic zinc blende structure with space group *F-43m*, has a bulk band gap of 3.37 eV and exciton binding energy of 60 meV at room temperature (RT).[12] The applications of ZnO are dependent on their intrinsic properties which are strongly correlated to the crystal structure, particle size, morphology and defect structure.[13–15] Lattice imperfections such as Schottky and Frenkel defects due to ion vacancies or interstitials, respectively change the cell volume and induce lattice strain. When the dimensions of the particles are reduced to nanometer size, high surface area to volume ratio and high concentration of defects such as grain boundaries, dislocations and surface states create a major impact on their optical and electrical properties. Instead of forfeiting the properties to the inevitable defects in ZnO nanostructures, the electronic and optical properties can be controlled if the defect centers are tuned and the role of intrinsic point defects such as cation/anion vacancies and interstitials are well understood.[16–19] Defects can be systematically introduced into the material by quenching the samples from high reaction temperatures within a narrow time window in different quenching media.[20] This allows fine-tuning the type and concentration of defects and helps in adjusting the microstructure of the material for luminescence to occur at specific wavelengths. The initial temperature from where the sample is quenched determines the native point defects which again alter the free electron density in the semiconductor.[21] The size and morphology of the nanostructures also influence the type of defect centers, which can be probed by the PL spectra.[22,23]

The characteristic emissions of ZnO in the UV region are recognized as the band edge transition or exciton recombination.[24–26] When photons with energies greater than the band gap energy are absorbed, the electrons populate the quasi-continuum states above the conduction band from where they relax to the conduction band

---

[*] Author to whom correspondence should be addressed.
Email: sayanb@iiserkol.ac.in

[†] These two authors contributed equally to this work.

Received: 2 January 2014
Accepted: 28 January 2014

1947-2935/2014/6/1160/010 doi:10.1166/sam.2014.1881

and thereafter to the defect levels.[27] In ZnO, the emissions from the intrinsic or extrinsic defect energy levels to the valence band occur in the visible region of the spectrum.[18] The observed emission bands depend on the excitation wavelength, temperature and different morphologies of ZnO nanostructures.[28] In addition, extended defects such as grain boundaries, dislocations and surface states in ZnO nanostructures lead to non-radiative centers which can decrease the quantum yield.[29] Intrinsic defects can be introduced by high temperature annealing or exposing ZnO samples to toxic vapors,[30,31] whereas extrinsic defect centers occur due to doping transition metal ions at the Zn^{2+} lattice sites.[32–34] The rate of heating of the precursors also controls the defect concentrations in the ZnO lattice, the faster the rate, higher are the defects.[35]

To utilize the ZnO nanostructures in practical devices, it is desirable to quantitatively tune the defect related emissions in the visible range. Also, the assemblage of nanoparticles into bigger sub-micron or micron-sized structures for fabrication purposes is an issue and requires a suitable template.[36] In this work, we utilized the thermal decomposition of zinc acetate dihydrate to synthesize 8–10 nm ZnO nanoparticles self-assembled into sub-micron clusters in one step. The defects were introduced by rapid cooling from 900 °C to air (27 °C), ice (0 °C) and liquid nitrogen (−196 °C) traps. Quantitative analyses of the lattice defects were performed by Rietveld analysis of X-ray diffraction (XRD) patterns. The types of defect emissions and the resulting optical properties were analyzed using RT PL spectra and electron transfer to carbon nanowhiskers (CNWs). The aim is to quantitatively estimate the type of defects in ZnO nanoparticle clusters, induced by a straight-forward quenching mechanism and their influence on the optical properties.

Delivered by Publishing Technology to: Sayan Bhattacharyya
IP: 14.139.220.33 On: Wed, 08 Oct 2014 09:24:41
Copyright: American Scientific Publishers

2. EXPERIMENTAL DETAILS

2.1. Materials

Zinc acetate dihydrate ($(CH_3COO)_2\ Zn \cdot 2H_2O$, Merck, 98%) was used without further purification.

2.2. Methodology

For all the samples, the heating protocol was similar and the samples differed in the way they were cooled to RT.

2.2.1. Z-P

1 g of $(CH_3COO)_2\ Zn \cdot 2H_2O$ was placed in an alumina boat and heat treated in air inside a tube furnace (Carbolite, single zone, model MTF 12/38/400) at 900 °C for 6 h at the rate of 6.5 °C/min. After 6 h, the sample was allowed to cool at the rate of 1.5 °C/min up to RT. The sample was named as pristine ZnO (Z-P).

2.2.2. Z-A

After heating 1 g of $(CH_3COO)_2\ Zn \cdot 2H_2O$ at 900 °C for 6 h, the red hot alumina boat containing the sample was taken out from the furnace and kept at ambient atmosphere. The sample cooled to RT within 20 min. It was assigned as air quenched ZnO (Z-A).

2.2.3. Z-I

After heating 1 g of $(CH_3COO)_2\ Zn \cdot 2H_2O$ at 900 °C for 6 h, the red hot alumina boat was taken out from the furnace and the sample was placed in an ice bath for 10 min. The sample was separated from the melted ice by centrifugation, after which it was dried at RT. The sample was called ice quenched ZnO (Z-I).

2.2.4. Z-LN

At first an ice trap was prepared and liquid nitrogen was poured inside the trap, which did not allow the liquid nitrogen to escape. After 6 h heating at 900 °C, the alumina boat containing ZnO was immersed into the trapped liquid nitrogen. Within 2 min liquid nitrogen evaporated and the quenched sample was transferred from the bath into air atmosphere. The liquid nitrogen quenched sample was named Z-LN.

2.2.5. CNWs

CNWs were synthesized by the pressure assisted conversion of waste mustard oil at high temperature, using the method described elsewhere.[37]

2.3. Characterization Techniques

Field emission scanning electron microscope (FESEM) images were recorded in Carl Zeiss SUPRA 55VP FESEM. Energy dispersive analysis of X-ray (EDAX) studies were performed with the Oxford Instruments X-Max with INCA software coupled to the FESEM. Transmission electron microscopy (TEM) images were obtained by UHR-FEG-TEM, JEOL, JEM 2100 F model using 200 keV electron source. The XRD measurements were carried out with a Rigaku (mini flex II, Japan) powder X-ray diffractometer having Cu $K\alpha = 1.54059$ Å radiation. Rietveld analysis of the XRD patterns was performed by the General Structure Analysis System (GSAS) software, Los Alamos National Laboratory Report (2004). The Fourier transform infrared (FTIR) measurements were carried out with a Perkin Elmer spectrum RX1 with KBr pellets. Each pellet contained 3 mg of the sample and 200 mg of KBr (FTIR grade). The electron paramagnetic resonance (EPR) spectra were recorded with a JEOL instrument. PL spectra were measured with Horiba Scientific Fluoromax-4 spectrofluorometer using a Xe lamp as the excitation source with a wavelength of 309 nm.

3. RESULTS AND DISCUSSION

3.1. Characterization by Scanning Electron Microscopy

The low magnification FESEM images as presented in the first column of Figure 1, indicate that all the samples Z-P,

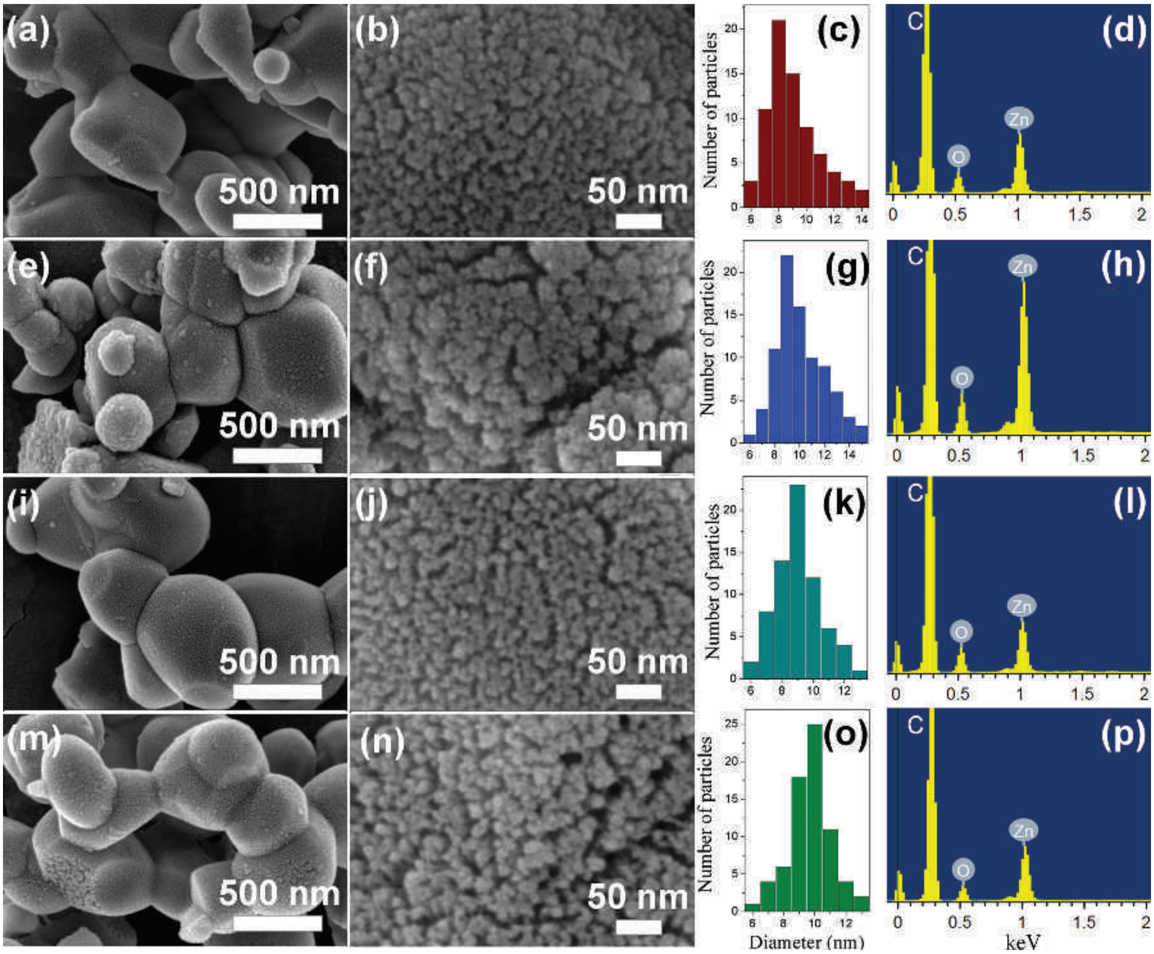

Fig. 1. Low and high magnification FESEM images, diameter histograms and EDAX patterns of Z-P (a)–(d), Z-A (e)–(h), Z-I (i)–(l) and Z-LN (m)–(p), respectively.

Z-A, Z-I and Z-LN consist of 200–500 nm grains (clusters) aggregated to each other. Higher magnification of these clusters revealed the presence of smaller grains, consisting of individual nanoparticles (second column of Fig. 1). In absence of quenching, the 20–25 nm smaller grains of Z-P were uniformly spaced. Bigger clusters were observed in Z-A where the grains were 25–50 nm. In Z-I and Z-LN, the smaller grains were 25–30 nm and irregularly spaced. The irregular spacing of the smaller grains implies larger fraction of grain boundaries in the defect bound ZnO samples. The third column of Figure 1 presents the diameter histogram of the ZnO nanoparticles, considering 70–80 particles in the ensemble. The particles in Z-P had an average size of 8 nm, Z-A and Z-I had ∼9 nm, and Z-LN consisted of ∼10 nm particles. The purity of the samples was confirmed from EDAX analyses, without any noticeable trace of foreign impurities.

3.2. Characterization by Transmission Electron Microscopy

TEM images provide a two-dimensional overview of the structural details in Figure 2. The 200–300 nm thick rod-like structures of Z-P could be observed in Figure 2(a), which was primarily due to the chain-like ordering of the sub-micron clusters (Fig. 1(a)). A closer view of the edges reveals the presence of individual nanoparticles. Figure 2(b) shows the high resolution (HR) TEM image of the highly crystalline Z-P where lattice fringes of the nanoparticles was observed. The difference in contrast distinguishes the individual nanoparticles and the dotted circle indicates one nanoparticle with a diameter in good agreement with the histograms obtained from SEM imaging (Fig. 1(c)).

Major discontinuities were not evident in the entire volume of Z-P, which clarifies the minimal presence of lattice deformations. The plot profile (Fig. 2(c)) and the FFT pattern in Figure 2(d) highlights the interplanar spacing to be 0.28 nm corresponding to the (100) reflection of the hexagonal crystal structure. Low resolution TEM image (Fig. 2(e)) of the representative quenched sample, Z-I shows the darker contrast of the nanoparticles dispersed over the matrix. The HR-TEM image of Z-I (Fig. 2(f)) is very informative and provides a visual evidence of the defects in the sample. 1–3 nm dispersed obstructions in the

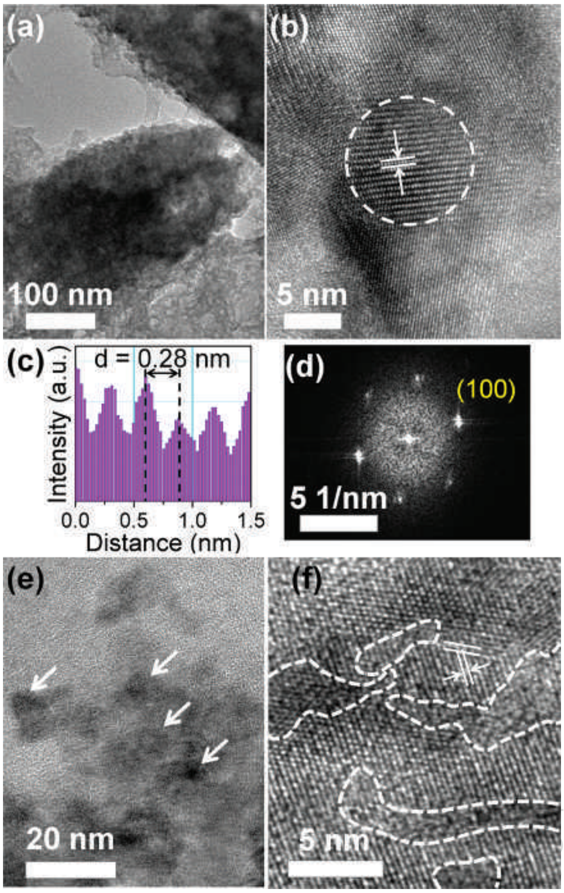

Fig. 2. (a) TEM image of Z-P, (b) HR-TEM image of Z-P showing the lattice fringes. The dotted circle highlights a spherical particle. (c) Plot profile of (b), demonstrating the interplanar spacing. (d) A typical FFT pattern showing the (100) reflection. (e) TEM image of representative Z-I. The arrows indicate the individual particles. (f) HR-TEM image of Z-I, showing the presence of topological defects, embedded inside dotted lines.

lattice fringes were observed which could be attributed to the grain boundaries and dislocations, percolating through the nanoparticles. The interplanar spacing of Z-I was also estimated to be 0.28 nm. The dislocations and grain boundaries should give rise to lattice strain which is a measure of the distribution of *a* and *c* lattice parameters.[38]

3.3. Formation of the Clustered Nanoparticles

The methodology involving high temperature decomposition of zinc acetate dihydrate was adapted to synthesize the self-assembled ZnO nanoparticles in one step. When heat treated in air, zinc acetate dihydrate undergoes dehydration and decomposition, through the intermediate formation of basic zinc acetate [$Zn_4O(CH_3COO)_6$] and acetic acid, and further elimination of CO_2 and acetone.[39] The one-step, straight forward synthesis methodology resulted in these self-assembled and clustered nanoparticles with a narrow size distribution, in direct contrast to the monodispersed ZnO particles prepared by wet-chemical routes.[40] The nucleation of the nanoparticles at lower temperatures was followed by clustering at 900 °C. Instead of growing in size, the particles retained their nanosize features, even in the absence of any surfactant or surface passivating layer. There are of course several instances of forming ZnO nanostructures by thermal decomposition of zinc acetate under ambient pressure, where the defects on the substrate act as nucleation sites.[39, 41, 42] Under high pressure conditions, the acetate groups however form a carbon coating on the 30–50 nm semiconductor nanocrystals.[33, 43, 44] Because of the close association of the nanoparticles and higher ionic nature at the surface of the nanoparticles than at the core, the surface defects are expected to play a major role in controlling the interfacial electronic structure and charge-transfer across the grain boundaries.[1] 900 °C was selected since a significant temperature difference with the quenching media was necessary to induce defects by breaking the long range translational symmetry of the crystalline structure in ZnO. Z-P and Z-A were cooled through a temperature difference of 873 °C, Z-I and Z-LN through 900 and 1096 °C, respectively.

3.4. XRD-Rietveld Analysis and Estimation of Defect%

The lattice imperfections present in thermal equilibrium were quantitatively analyzed by studying the changes in the lattice parameters and cell volume. All the samples crystallized in the hexagonal crystal structure with $P6_3mc$ space group. Figure 3 shows the Rietveld refinement of the XRD patterns and the fitted parameters are tabulated in Table I. The atomic positions of the O^{2-} ions were found to be slightly shifted along the z-axis due to the lattice disorder induced by quenching. The increase in *a* and *c* parameters of Z-A, Z-I and Z-LN with respect to Z-P were 0.0098(0), 0.011(0), 0.014(0)% and 0.015(0), 0.0182(1), 0.0176(1)%, respectively (Fig. 4(a)). The corresponding percent increase in cell volume of Z-A, Z-I and Z-LN was 0.036(1), 0.042(1) and 0.046(1), respectively with respect to Z-P.

echnology to: Sayan Bhattacharyya
n: Wed, 08 Oct 2014 09:24:4
rican Scientific Publishers

To estimate the defect% based on the changes in cell volume (V),[45] the density of atoms (D in g/cm^3) inside the lattice for each sample was calculated using the relation $D = (\text{Number of atoms in the unit cell} * \text{Molecular mass of ZnO})/(V * N_A)$, where N_A is the Avogadro's number. The atomic densities calculated for Z-P, Z-A, Z-I and Z-LN were 11.3411(1), 11.3371(2), 11.3364(1) and 11.3359(0) g/cm^3, respectively which are double than 5.6 g/cm^3,[46] the density of ZnO obtained from the table of physical constants of inorganic compounds. This clearly implies the presence of defects and lattice imperfections in the synthesized ZnO nanoparticle clusters, irrespective of quenching. When compared to the lattice parameters of other ZnO systems, the cell volume appears to be of the same order of magnitude viz. 11.3583 (JCPDS 89-0511), 11.3468 (JCPDS 79-2205) and 11.3652 g/cm^3 (JCPDS 89-0510). The defect% was calculated from the percentage change in D.

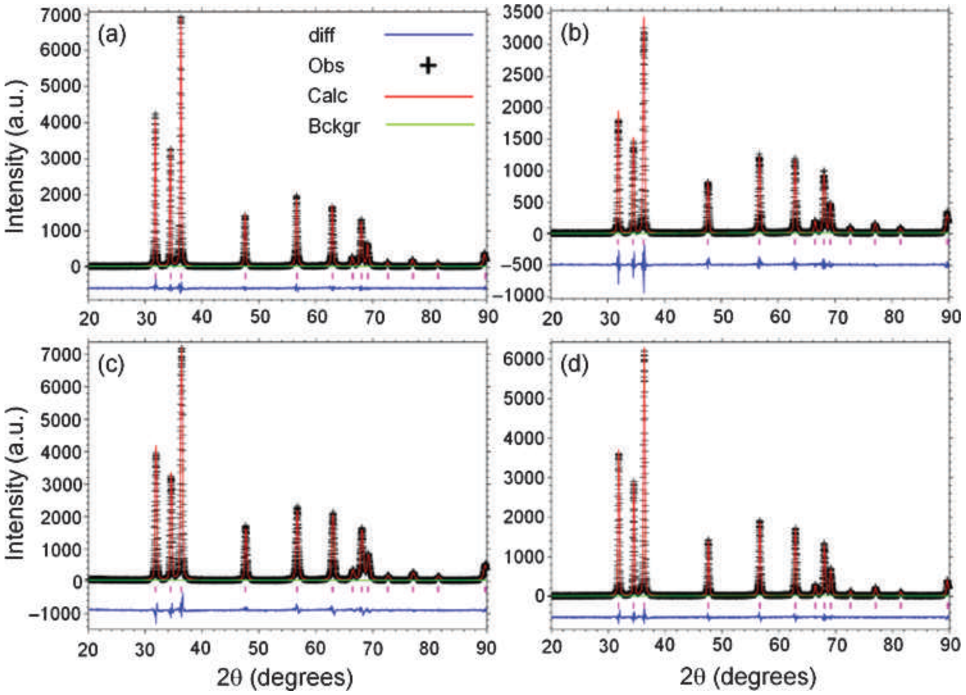

Fig. 3. XRD-Rietveld analysis patterns of (a) Z-P, (b) Z-A, (c) Z-I and (d) Z-LN. The legends: *diff* (difference plot between observed and calculated patterns; *Obs* (observed pattern); *Calc* (calculated pattern); and *Bckgr* (background plot).

Delivered by Publishing Technology to: Sayan Bhattacharyya
IP: 14.139.220.33 On: Wed, 08 Oct 2014 05:24:41
Copyright: American Scientific Publishers

Figure 4(b) shows the trend of increase of defect% of the quenched samples with respect to Z-P i.e., 0.035(1), 0.044(0) and 0.053(0)% for Z-A, Z-I and Z-LN, respectively. A similar trend was observed with respect to the density of atoms from other reported JCPDS files. It clearly shows that the normal cooled sample Z-P also had 0.15–0.21% lattice imperfections as compared to the reported standard ZnO lattices, mainly due to the surface defects in the clustered nanoparticles.

3.5. Fourier Transform Infrared Spectroscopy

The representative room temperature FTIR spectrum of Z-P is presented in Figure 4(c). The bands at 3434 and 1627 cm^{-1} correspond to the stretching and bending vibrations of the hydroxyl groups attached to the nanoparticles. The functional groups from zinc acetate dihydrate would not exist at 900 °C, and hence these bands can be attributed to the physisorbed H_2O molecules on the nanoparticle cluster surface. The vibration of interest is the strong band

Table I. XRD-rietveld refinement parameters.

Sample [space group]	Lattice parameters (Å); Angles (°); Cell volume (Å^3)	Atomic positions (x, y, z)	Occupation number	Weighted profile (R_{wp}) (%)
Z-P [$P6_3mc$]	$a = b = 3.25074$ Å $c = 5.20732$ Å $\alpha = \beta = 90°$, $\gamma = 120°$ $V = 47.655$ Å^3	Zn1 (0.333, 0.667, 0.000) O2 (0.333, 0.667, 0.383)	Zn1 = 1.0 O2 = 1.0	10.36
Z-A [$P6_3mc$]	$a = b = 3.25106$ Å $c = 5.20810$ Å $\alpha = \beta = 90°$, $\gamma = 120°$ $V = 47.672$ Å^3	Zn1 (0.333, 0.667, 0.000) O2 (0.333, 0.667, 0.383)	Zn1 = 1.0 O2 = 1.0	13.79
Z-I [$P6_3mc$]	$a = b = 3.25110$ Å $c = 5.20827$ Å $\alpha = \beta = 90°$, $\gamma = 120°$ $V = 47.675$ Å^3	Zn1 (0.333, 0.667, 0.000) O2 (0.333, 0.667, 0.384)	Zn1 = 1.0 O2 = 1.0	10.25
Z-LN [$P6_3mc$]	$a = b = 3.25120$ Å $c = 5.20824$ Å $\alpha = \beta = 90°$, $\gamma = 120°$ $V = 47.677$ Å^3	Zn1 (0.333, 0.6662, 0.000) O2 (0.333, 0.667, 0.385)	Zn1 = 1.0 O2 = 1.0	10.97

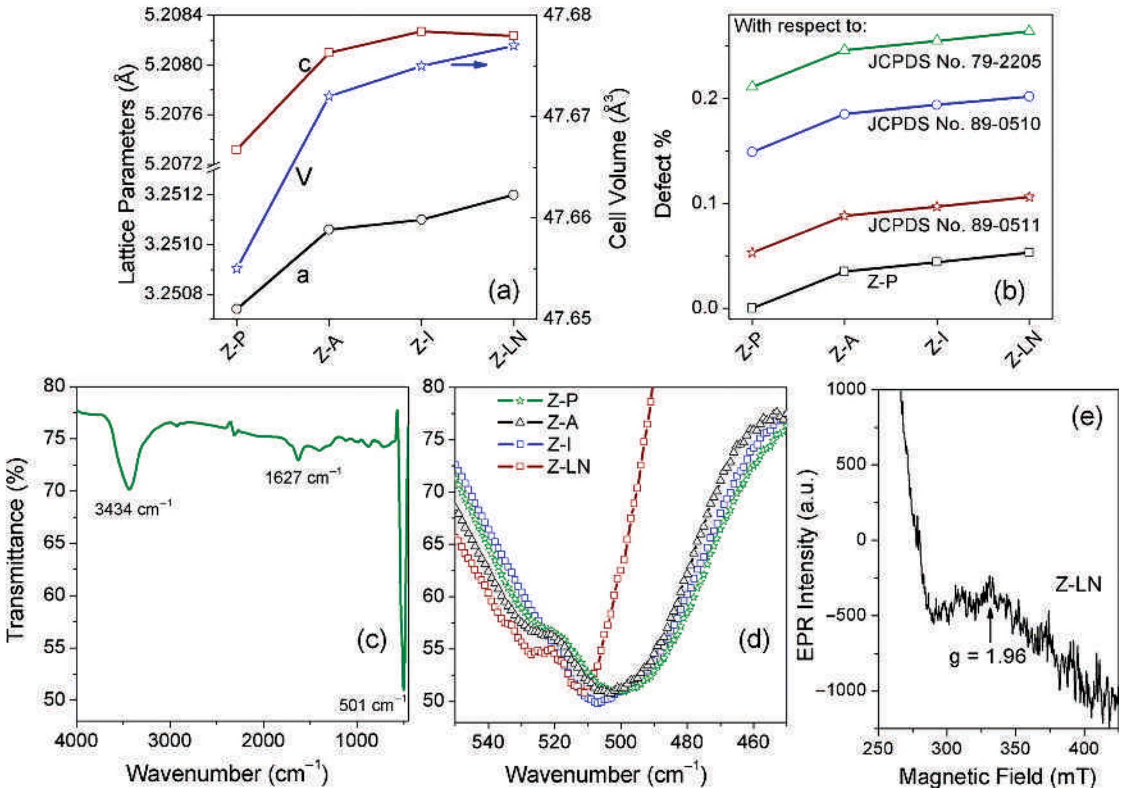

Fig. 4. Plots of (a) lattice parameters (a), (c), cell volume (V) and (b) defect%. FTIR spectra of: (c) Z-P, and (d) Zn-O stretching band. (e) EPR spectrum of Z-LN.

Delivered by Publishing Technology to: Sayan Bhattacharyya
IP: 14.139.220.33 On: Wed, 08 Oct 2014 09:24:41
Copyright: American Scientific Publishers

at 501 cm^{-1} which corresponds to the longitudinal-optical (LO) component of A_1 mode of Zn-O.[47] This vibrational frequency shifts to 503, 507 and 511 cm^{-1} in Z-A, Z-I and Z-LN, respectively as depicted in Figure 4(d). The wavenumber ($\bar{\nu}$) of a bond is inversely related to the bond force constant (k) by the relation: $\bar{\nu} = (1/2\pi c)\sqrt{(k/\mu)}$, where c is the velocity of light and μ is the reduced mass. Higher bond strengths will result in higher k, which will shift the particular band to higher wavenumber. Z-P and Z-A had close Zn-O frequencies whereas Z-I and Z-LN were in nearby range, which points to the role of temperature of the quenching medium. The lattice degrees of freedom were in a non-equilibrium state at the ice and liquid nitrogen temperatures, and the atomic positions of the Z-I and Z-LN lattice equilibrated when both Z-I and Z-LN returned to RT. The non-equilibrium low temperatures of ice and liquid nitrogen could arrest the vibration of the Zn-O bond, which give rise to higher coulombic attraction between Zn^{2+} and O^{2-} ions and lowers the entropy, increasing the bond strength. The A_1 (LO) mode of Zn-O in Z-LN had lowest entropy and highest bond strength at the non-equilibrium liquid nitrogen temperature, which could relax after returning to RT. However even after equilibration of the Zn-O bonds at RT, the bond strength could not be lowered down to that of Z-P and Z-A. In spite of increasing bond strengths, the increase of lattice cell volume from Z-P, Z-A to Z-I and Z-LN could be satisfactorily explained by the existence of vacancies and interstitials in the ZnO lattice.

The trends in defect concentration obtained from Rietveld refinement of the XRD patterns and FTIR spectra resemble the quench-induced structural disorder. The disorder increased with larger temperature difference between the initial (900 °C) and final non-equilibrium states. In Z-P, both the lattice and spin degrees of freedom could relax upon cooling from 900 °C to RT over a period of 9.7 h and thus the Zn-O bond lengths and Zn-O-Zn bond angles could achieve thermodynamic equilibrium with minimum concentration of defects. When Z-A was quenched in air, cooling occurred at a faster rate of ~44 °C/min, which disrupted the long-range crystalline ordering. In Z-I and Z-LN, even after thermal equilibration of the defects at RT, the structural heterogeneities have an infinite lifetime.[48] The defects were kinetically created and pinned by the induced disorder and hence they could be characterized by various techniques.

3.6. Electron Paramagnetic Resonance Spectrum

Figure 4(e) shows the EPR spectrum of Z-LN recorded at liquid nitrogen temperature. In the supposedly diamagnetic ZnO, the low-field signal with g-factor close to the free-electron value ($g = 2.0023$) is generally attributed to oxygen vacancy (V_o) with a trapped unpaired electron.[49] This peak is surprisingly absent in Z-LN and rather a high-field signal at $g = 1.96$ was observed. This high-field peak was attributed to the presence of zinc interstitials (Zn_i). The EPR result matches very well with the PL spectra.

3.7. Optical Properties

PL spectra were recorded and the data fitted with the most reasonable number of sub-peaks to study the type of induced defects and their influence on the optical properties. The emission bands were fitted by multiple Gaussian peak functions with optimal full width at half maxima (FWHM). Figure 5 shows the RT PL spectra and energy band diagrams of ZnO samples obtained with excitation wavelength (λ_{ex}) of 309 nm and the corresponding parameters from multi-peak fitting are tabulated in Table II. The presence of multiple peaks in the visible region of the electromagnetic spectrum is typical for nanocrystalline ZnO.[50] The spectra reveal a band edge emission centered at 352–356 nm and a broad emission ranging from 375 to 600 nm centered at 413–416 nm. The band edge peaks at 353, 356, 355 and 353 nm for Z-P, Z-A, Z-I and Z-LN, respectively are blue shifted as compared to that of bulk ZnO (368 nm) which is due to quantum confinement effect.[23] Z-P and Z-A displayed three violet emissions and one blue emission, whereas for Z-I and Z-LN, all the emission peaks were observed in the violet region (Table II). Theoretically, the Zn_i, V_{zn} and oxygen interstitial (O_i) energy levels are located ~0.22, ~3.06 and ~2.28 eV below the conduction band, respectively whereas V_o level is ~0.9 eV above the valence band.[51] The deep level emissions occur in the green (~2.5 eV) and orange-red (~1.95 eV) region, which are absent in our ZnO samples. The violet emission usually originates from the Zn_i defects, where electronic transition occurs from Zn_i level to valence band.[32,51] Blue emission is due to the transition from Zn_i level to V_{zn} states. The presence of more than one violet emissions could be due to the different shallow energy levels in close vicinity inside the band gap (Fig. 5), associated with interface trap in the grain boundaries,[52] and dislocations.[53] Also, the coexistence of interstitial sites with different energy configurations such as isolated or split interstitials is highly possible, which can result in closely spaced energy levels.[54]

hnology to: Sayan Bhattacharyya
Wed, 08 Oct 2014 09:24:41
an Scientific Publishers

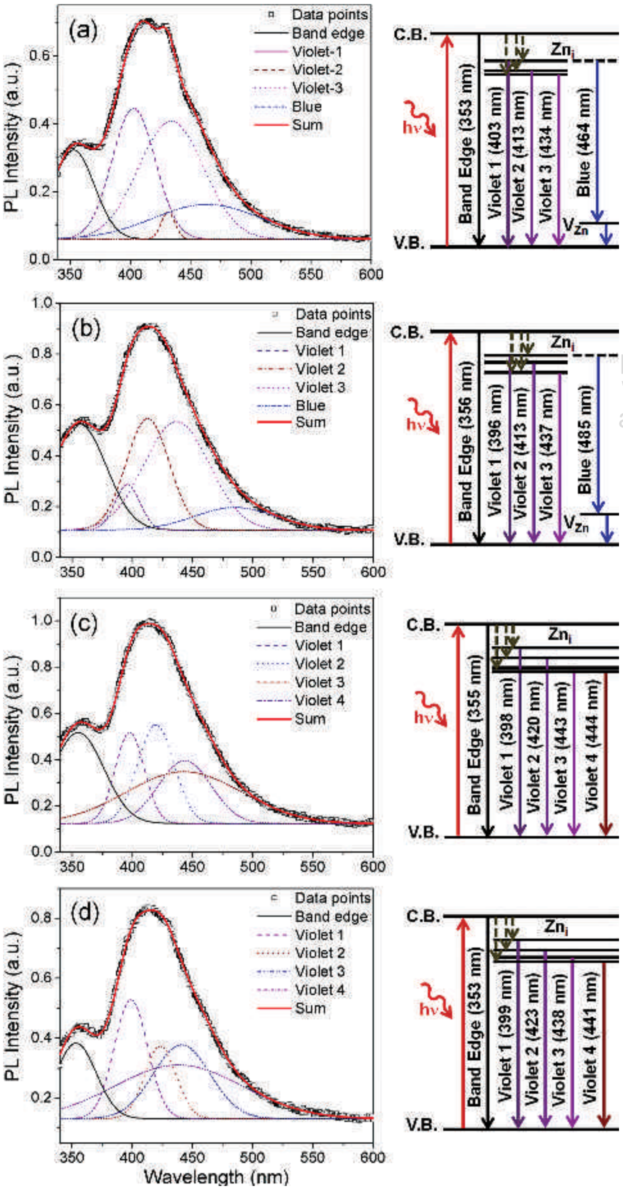

Fig. 5. Room temperature PL spectra and the corresponding simplified energy band diagrams of (a) Z-P, (b) Z-A, (c) Z-I and (d) Z-LN. The solid and dotted lines in the energy band diagram represent the radiative and non-radiative emission processes, respectively.

Table II. Parameters from multi-peak fitting of the room temperature PL spectra (BE = band edge, V = violet, B = blue).

Sample	Peaks (nm)	Bands	Absolute area (Counts · nm)	FWHM (nm)
Z-P	353	BE	11.4	34.6
	403	V1	17.3	35.8
	431	V2	1.2	11.5
	434	V3	23.7	54.2
	464	B	11.5	89.5
Z-A	356	BE	23.2	44.3
	396	V1	4.7	20.9
	413	V2	19.6	35.7
	437	V3	29.0	54.3
	485	B	7.6	67.7
Z-I	355	BE	21.0	42.6
	398	V1	11.9	24.2
	420	V2	16.2	30.2
	443	V3	26.9	96.0
	444	V4	14.9	43.8
Z-LN	353	BE	10.6	33.4
	399	V1	13.8	27.7
	423	V2	7.9	26.1
	438	V3	23.8	106.0
	441	V4	14.7	47.5

Considering the area under the peaks, it can be observed from Table II that in all the samples, the low lying energy levels corresponding to the 434–485 nm bands were mostly populated. As observed from Figure 5, the energy band diagrams of Z-P and Z-A are identical, so do Z-I and Z-LN. The higher intensities of V2 and V3 emissions in Z-A as compared to Z-P was due to the larger agglomeration in Z-A (Fig. 1(e)) resulting in higher concentration of grain boundaries, dislocations and surface traps. The blue emission could also arise from the surface deep traps apart from the Zn_i to V_{Zn} transition in Z-P and Z-A.[50] The surface traps were preferentially removed by the quenching process in Z-I and Z-LN and hence the blue emission was not observed. The band edge emission in Z-I and Z-LN was 23 and 15%, respectively as compared to the area of the violet emissions, which clearly indicates higher concentration of Zn_i sites in Z-LN. Interestingly, the green emission typical for V_o was not observed in our samples, which was corroborated by the absence of any paramagnetic signal at $g = 2.0023$ in the EPR spectrum (Fig. 4(e)).[55] There are few other cases in the literature, where the green emission from V_o defects was not observed and the PL spectra were dominated by violet and blue emissions induced by doping,[56,57] and treatments such as laser ablation, H-plasma and atomic layer deposition.[58–60]

3.8. Electron Transfer to Carbon Nanowhiskers

When the photons are absorbed, the self-assembled ZnO nanoparticles undergo charge separation, whereby a majority of e^{-}–h^{+} recombination take place and a fraction of these charge carriers remain trapped at the defect sites. In the presence of a second species with different Fermi energy level, charge equilibration and electron transfer can occur from the donor (ZnO) to the acceptor species through a non-radiative pathway.

Delivered by Publishing Technolo
IP: 14.139.220.33 On: Wed,
Copyright: American Sc

The electron transfer can be probed by a decrease in PL intensity of ZnO with increasing concentration of the second species such as carbon nanotubes or conjugated dye.[61,62] This process underlines the principle behind photochemical solar cells.[63] We have used ethanol dispersions of CNW and ZnO nanoparticle clusters to evaluate the electron transfer dynamics from the latter to the CNWs consisting of a mixture of sp^2 and sp^3 hybridized carbon.[37] The objective of this exercise was to understand whether electron transfer will take place only from the conduction band of ZnO or also from the defect levels. The relative PL quenching of the bands with increasing CNW concentration should give an estimate of the Fermi level of the electron scavenger (CNW). Since the CNWs has no detectable absorption in the visible range, spectroscopic evidence of electrons residing in the CNWs was not obtained. Figures 6(a)–(d) shows PL intensity quenching of the ZnO samples with 0–0.2 mg/mL CNW concentrations. The band edge and defect emissions were proportionately quenched by non-radiative electron transfer to the Fermi level of the CNW (Fig. 6(e)). The excited state deactivation was nearly complete with 0.2 mg/mL CNWs. Figures 7(a), (c), (e) and (g) show the changes in area under the peak for each emission band with increasing CNW concentration. This enables comparison between the PL quenching rates from the different excited states. The representative PL spectra with 0.1 mg/mL CNWs are shown in Figures 7(b), (d), (f) and (h). From the fitted PL spectra it was observed that some of the emission bands were increasingly red-shifted with increasing concentration of CNWs. The CNWs provide support for adherence of the ZnO nanoparticles, the latter coalesced and grew in size, leading to the observed red shift.

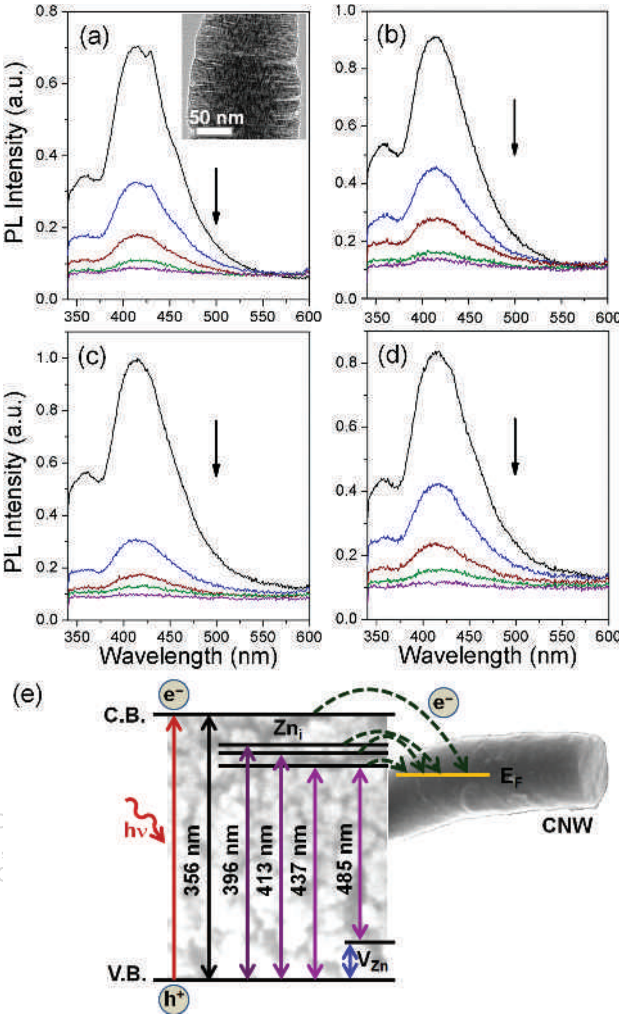

Fig. 6. Quenching of PL intensity of (a) Z-P, (b) Z-A, (c) Z-I and (d) Z-LN in ethanol (1 mL) recorded during addition of 0, 0.05, 0.1, 0.15 and 0.2 mg/mL CNWs; $\lambda_{ex} = 309$ nm. The arrows indicate the increasing concentration of CNW. (Inset of a) TEM image shows the cross section of CNW. (e) Schematic band diagram showing the electron transfer from the conduction and defect bands of Z-A to the Fermi level of CNW.

From Figure 7(a), it is evident that in Z-P, the V2 emission (423–431 nm) was minimum as compared to Z-A, Z-I and Z-LN (Figs. 7(c), (e), (g)) and hence the intensity of this band in Z-P did not change significantly with CNWs, unlike the quenched samples. Thus it can be inferred that

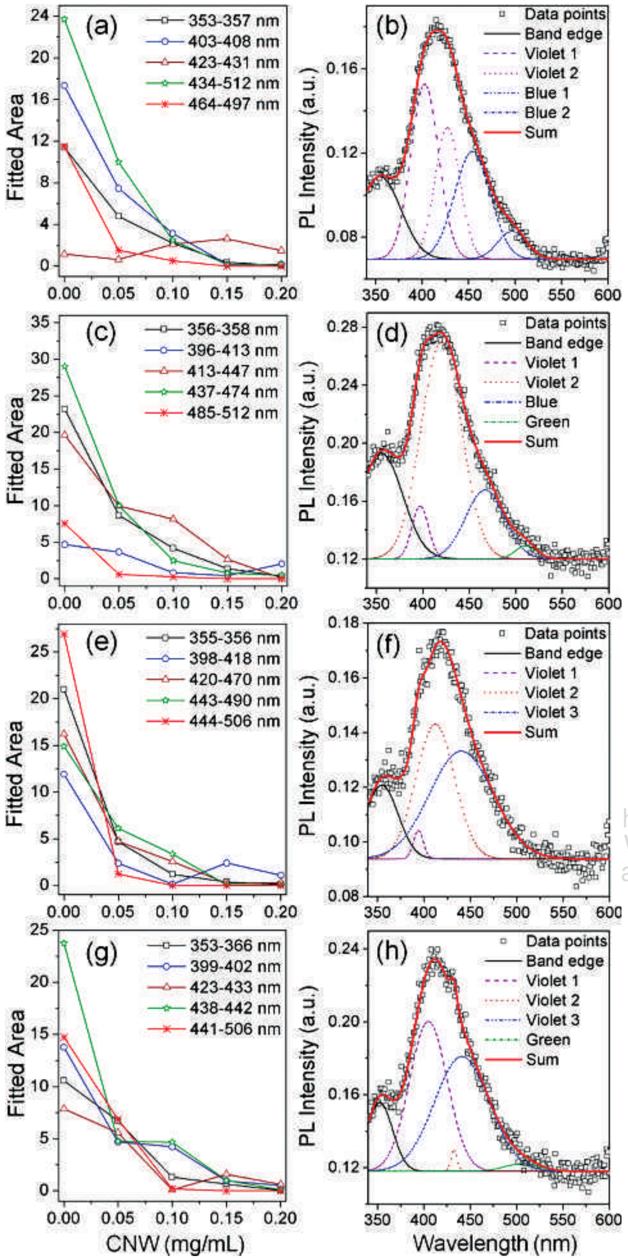

Fig. 7. Plots of fitted area versus CNW concentration for the different bands (left column) and the representative fitted PL spectra after addition of 0.1 mg/mL CNW (right column) for (a), (b) Z-P, (c), (d) Z-A, (e), (f) Z-I and (g), (h) Z-LN, respectively.

the defect state corresponding to the V2 band was induced in Z-A, Z-I and Z-LN as a result of quenching and can be attributed to the increased percentage of dislocations and grain boundaries in the quenched samples. The blue emission in Z-P (464–497 nm) and Z-A (485–512 nm) was quenched faster as compared to the other emission bands and was almost quenched at 0.05 mg/mL CNWs. Similarly the V4 emission in Z-I (444–506 nm) and Z-LN (441–506 nm) was almost quenched at 0.1 mg/mL CNWs. Thus the emission bands from the lowest energy levels were completed quenched by the CNWs.

Highest electron transfer rates are possible when the donor and acceptor Fermi energy levels get equilibrated and hence the Fermi level of the CNWs could be depicted as shown in Figure 6(e). Hence, with a certain electron acceptor, the dynamics of electron transfer can be controlled if the defect levels of the semiconductor donor can be tuned by quenching in different media. If the defect states are bound to grain boundaries, dislocations or surface traps, the electrons associated with the excited defect states are quenched faster. In contrast, the slower quenching dynamics of the defect bands associated with point defects in the lattice, such as Zn_i, can be envisaged from the non-disappearance of V1 emission even at 0.10–0.15 mg/mL CNWs in Z-I and Z-LN.

4. CONCLUSIONS

In summary, structural defects were induced in 8–10 nm ZnO nanoparticles self-assembled into sub-micron clusters by thermal decomposition of zinc acetate dihydrate at 900 °C and subsequent quenching from high temperature to air, ice and liquid nitrogen. The results can be summarized point wise as: (1) The cell volume and defect% of air, ice and liquid nitrogen quenched samples increased by 0.036(1), 0.042(1) and 0.046(1)%, respectively with respect to the pristine ZnO sample. A continuous increase in disorder and higher Zn-O bond strength was observed with larger temperature difference between 900 °C and the quenching media. (2) HR-TEM imaging enabled direct visualization of the grain boundaries/dislocations induced by quenching. (3) The pristine and air quenched sample showed three violet emissions and one blue emission, whereas the ice and liquid nitrogen quenched samples displayed four emission peaks in the violet region, which indicates the presence of only zinc interstitials and zinc vacancies and absence of any oxygen vacancy. (4) Multiple violet emissions can be attributed to zinc interstitials as well as different shallow energy levels associated with interface trap in the grain boundaries and dislocations. (5) The electron transfer from the ZnO nanoparticle clusters to the carbon nanowhiskers was probed and it was observed that the band edge and defect bands simultaneously take part in the process. The defect state corresponding to 413 nm (V2 emission) was induced due to higher grain boundaries and dislocations in the quenched samples. Also, the emission bands from the lowest energy levels were completed quenched by carbon. Our approach enabled the quantitative tuning of defect states and hence the corresponding emissions of ZnO clustered nanoparticles.

hnology to: Sayan Bhattacharyya
Wed, 08 Oct 2014 09:24:41
an Scientific Publishers

Acknowledgment: The authors thank Subhasis Sinha for useful discussion and Abheek Datta for providing the carbon nanowhiskers. Bharati Debnath wishes to thank Anustup Sadhu for Rietveld refinement training. Bharati Debnath and Ganga Halder thank DST-INSPIRE programme and University Grants Commission (UGC), New Delhi for their fellowships, respectively. The Science and Engineering Research Board (SERB) of Department of Science and Technology (DST), India is duly acknowledged for the financial support under sanction no. SR/S1/PC-28/2011.

References and Notes

1. H. Li, L. K. Schirra, J. Shim, H. Cheun, B. Kippelen, O. L. A. Monti, and J.-L. Bredas, *Chem. Mater.* 24, 3044 (**2012**).

2. M. H. Huang, S. Mao, H. Feick, H. Yan, Y. Wu, H. Kind, E. Weber, R. Russo, and P. Yang, *Science* 292, 1897 (**2001**).

3. M. Chen, Z. Wang, D. Han, F. Gu, and G. Guo, *J. Phys. Chem. C* 115, 12763 (**2011**).

4. M. Dutta, S. Sarkar, T. Ghosh, and D. Basak, *J. Phys. Chem. C* 116, 20127 (**2012**).

5. R. Zou, G. He, K. Xu, Q. Liu, Z. Zhang, and J. Hu, *J. Mater. Chem. A* 1, 8445 (**2013**).

6. J. Goldberger, D. J. Sirbuly, M. Law, and P. Yang, *J. Phys. Chem. B.* 109, 9 (**2005**).

7. P. Sharma, A. Gupta, K. V. Rao, F. J. Owens, R. Sharma, R. Ahuja, J. M. O. Guillen, B. Johansson, and G. A. Gehring, *Nat. Mater.* 2, 673 (**2003**).

8. T. Fukumura, Y. Yamada, H. Toyosaki, T. Hasegawa, H. Koinuma, and M. Kawasaki, *Appl. Surf. Sci.* 223, 62 (**2004**).

9. J. Wang, P. Liu, X. Fu, Z. Li, W. Han, and X. Wang, *Langmuir* 25, 1218 (**2009**).

10. S. Bhattacharyya and A. Gedanken, *J. Phys. Chem. C* 112, 13156 (**2008**).

11. X. Huang, X. Wang, S. Wang, J. Yang, L. Zhong, and J. Pan, *Nanoscale* 5, 5596 (**2013**).

12. Ü. Özgür, Y. I. Alivov, C. Liu, A. Teke, M. A. Reshchikov, S. Doan, V. Avrutin, S.-J. Cho, and H. Morkoç, *J. Appl. Phys.* 98, 041301-1 (**2005**).

13. G. Zhang and M. Liu, *Sens. Actuators, B* 69, 144 (**2000**).

14. A. P. Alivisatos, *J. Phys. Chem.* 100, 13226 (**1996**).

15. L. Zhang, X. Liu, C. Geng, H. Fang, Z. Lian, X. Wang, D. Shen, and Q. Yan, *Inorg. Chem.* 52, 10167 (**2013**).

16. D. Wang and C. Song, *J. Phys. Chem. B.* 109, 12697 (**2005**).

17. H. Huang, S. Yang, J. Gong, H. Liu, J. Duan, X. Zhao, R. Zhang, Y. Liu, and Y. Liu, *J. Phys. Chem. B.* 109, 20746 (**2005**).

18. J. Zhang, L. Sun, J. Yin, H. Su, C. Liao, and C. Yan, *Chem. Mater.* 14, 4172 (**2002**).

19. A. B. Djurišić and Y. H. Leung, *Small* 2, 944 (**2006**).

20. P. Supphasrirongjaroen, W. Kongsuebchart, J. Panpranot, O. Mekasuwandumrong, C. Satayaprasert, and P. Praserthdam, *Ind. Eng. Chem. Res.* 47, 693 (**2008**).

21. P. Fochuk, R. Grill, and O. Panchuk, *J. Electron. Mater.* 35, 1354 (**2006**).

22. X. Liu and M. T. Swihart, *Nanoscale* 5, 8029 (**2013**).

23. S. Bhattacharyya and A. Gedanken, *Micropor. Mesopor. Mater.* 110, 553 (**2008**).

24. Y. H. Yang, X. Y. Chen, Y. Feng, and G. W. Yang, *Nano. Lett.* 7, 3879 (**2007**).

25. N. W. Wang, Y. H. Yang, and G. W. Yang, *J. Phys. Chem. C* 113, 15480 (**2009**).

26. F. Leiter, H. Alves, D. Pfisterer, N. G. Romanov, D. M. Hofmann, and B. K. Meyer, *Phys. B.* 340–342, 201 (**2003**).

27. K. Tvrdy, P. A. Frantsuzov, and P. V. Kamat, *Proc. Natl. Acad. Sci. USA* 108, 29 (**2011**).

28. A. B. Djurišić, Y. H. Leung, K. H. Tam, L. Ding, W. K. Ge, H. Y. Chen, and S. Gwo, *Appl. Phys. Lett.* 88, 103107-1 (**2006**).

29. S. Chattopadhyay, S. K. Neogi, P. Pandit, S. Dutta, T. Rakshit, D. Jana, S. Chattopadhyay, A. Sarkar, and S. K. Ray, *J. Lumin.* 132, 6 (**2012**).

30. K. S. Babu, A. R. Reddy, Ch. Sujatha, K. V. G. Reddy, and A. N. Mallika, *Mater. Lett.* 110, 10 (**2013**).

31. R. Aad, V. Simic, L. L. Cunff, L. Rocha, V. Sallet, C. Sartel, A. Lusson, C. Couteau, and G. Lerondel, *Nanoscale* 5, 9176 (**2013**).

32. N. S. Sabri, A. K. Yahya, and M. K. Talari, *J. Lumin.* 132, 1735 (**2012**).

33. S. Bhattacharyya and A. Gedanken, *J. Phys. Chem. C* 112, 4517 (**2008**).

34. G. Srinet, R. Kumar, and V. Sajal, *J. Appl. Phys.* 114, 033912-1 (**2013**).

35. V. Ischenko, S. Polarz, D. Grote, V. Stavarache, K. Fink, and M. Driess, *Adv. Funct. Mater.* 15, 1945 (**2005**).

36. P. D. García and C. López, *J. Mater. Chem. C* 1, 7357 (**2013**).

37. A. Datta, P. Dutta, A. Sadhu, S. Maiti, and S. Bhattacharyya, *J. Nanopart. Res.* 15, 1808-1 (**2013**).

38. V. D. Mote, Y. Purushotham, and B. N. Dole, *J. Theor. Appl. Phys.* 6, 6 (**2012**).

39. C.-C. Lin and Y.-Y. Li, *Mater. Chem. Phys.* 113, 334 (**2009**).

40. C. Zhang, K. Li, S. Song, and D. Xue, *Chem. Eur. J.* 19, 6329 (**2013**).

41. X.-M. Chen, X.-Y. Gao, S. Zhang, and H.-T. Liu, *Acta Phys. Sinica* 62, 049102 (**2013**).

42. X. Su, Z. Zhang, Y. Wang, and M. Zhu, *J. Phys. D: Appl. Phys.* 38, 3934 (**2005**).

43. S. Bhattacharyya, D. Zitoun, and A. Gedanken, *J. Phys. Chem. C* 112, 7624 (**2008**).

44. S. Bhattacharyya, A. Pucci, D. Zitoun, and A. Gedanken, *Nanotechnology* 19, 495711 (**2008**).

45. H. Morkoç and U. Özgür, General Properties of ZnO in Zinc Oxide: Fundamentals, Materials and Device Technology, Wiley-VCH Verlag GmbH & Co. KGaA, Weinheim, Germany (**2009**), Chap. 1, p. 13.

46. D. R. Lide, CRC Handbook of Chemistry and Physics, CRC Press, Boca Raton, FL (**2003**).

47. Y. Zheng, C. Chen, Y. Zhan, X. Lin, Q. Zheng, K. Wei, J. Zhu, and Y. Zhu, *Inorg. Chem.* 46, 6675 (**2007**).

48. M. H. Vainstein, D. A. Stariolo, and J. J. Arenzon, *J. Phys. A: Math. Gen.* 36, 10907 (**2003**).

49. H. Zeng, G. Duan, Y. Li, S. Yang, X. Xu, and W. Cai, *Adv. Funct. Mater.* 20, 561 (**2010**).

50. S. Bhattacharyya and A. Gedanken, *J. Phys. Chem. C* 112, 659 (**2008**).

51. C. H. Ahn, Y. Y. Kim, D. C. Kim, S. K. Mohanta, and H. K. Cho, *J. Appl. Phys.* 105, 013502-1 (**2009**).

52. B. J. Jin, S. Im, and S. Y. Lee, *Thin Solid Films* 366, 107 (**2000**).

53. M. Peres, S. Magalhães, M. R. Soares, M. J. Soares, L. Rino, E. Alves, K. Lorenz, M. R. Correia, A. C. Lourenço, and T. Monteiro, *Phys. Stat. Sol. C* 10, 662 (**2013**).

54. A. R. West, Solid State Chemistry and its Applications, John Wiley & Sons, Singapore (**1989**).

55. C. Drouilly, J.-M. Krafft, F. Averseng, S. Casale, D. Bazer-Bachi, C. Chizallet, V. Lecocq, H. Vezin, H. Lauron-Pernot, and G. Costentin, *J. Phys. Chem. C* 116, 21297 (**2012**).

56. W.-J. Chen, J.-K. Wu, J.-C. Lin, S.-T. Lo, H.-D. Lin, D.-R. Hang, M. F. Shih, C.-T. Liang, and Y. H. Chang, *Nanoscale Res. Lett.* 8, 313-1 (**2013**).

57. S. Zhao, Y. Zhou, K. Zhao, Z. Liu, P. Han, S. Wang, W. Xiang, Z. Chen, H. Lü, B. Cheng, and G. Yang, *Physica B* 373, 154 (**2006**).

58. H. Zeng, Z. Li, W. Cai, and P. Liu, *J. Appl. Phys.* 102, 104307-1 (**2007**).

59. C. Chen, Y. Lu, H. He, M. Xiao, Z. Wang, L. Chen, and Z. Ye, *ACS Appl. Mater. Interfaces* 5, 10274 (**2013**).

60. M.-J. Chen, J.-R. Yang, and M. Shiojiri, *Semicond. Sci. Technol.* 27, 074005 (**2012**).

61. M. Dutta, S. Jana, and D. Basak, *ChemPhysChem* 11, 1774 (**2010**).

62. G. A. Beane, A. J. Morfa, A. M. Funston, and P. Mulvaney, *J. Phys. Chem. C* 116, 3305 (**2012**).

63. P. V. Kamat, *J. Phys. Chem. C* 111, 2834 (**2007**).

Delivered by Publishing Technology to: Sayan Bhattacharyya
IP: 14.139.220.33 On: Wed, 08 Oct 2014 09:24:41
Copyright: American Scientific Publishers